

Modeling the stability of polygonal patterns of vortices at the poles of Jupiter as revealed by the *Juno* spacecraft

Cheng Li^{a,1} , Andrew P. Ingersoll^b , Alexandra P. Klipfel^b , and Harriet Brettle^b

^aAstronomy Department, University of California, Berkeley, CA 94720; and ^bDivision of Geological and Planetary Sciences, California Institute of Technology, Pasadena, CA 91125

Edited by Neta A. Bahcall, Princeton University, Princeton, NJ, and approved August 3, 2020 (received for review April 30, 2020)

From its pole-to-pole orbit, the *Juno* spacecraft discovered arrays of cyclonic vortices in polygonal patterns around the poles of Jupiter. In the north, there are eight vortices around a central vortex, and in the south there are five. The patterns and the individual vortices that define them have been stable since August 2016. The azimuthal velocity profile vs. radius has been measured, but vertical structure is unknown. Here, we ask, what repulsive mechanism prevents the vortices from merging, given that cyclones drift poleward in atmospheres of rotating planets like Earth? What atmospheric properties distinguish Jupiter from Saturn, which has only one cyclone at each pole? We model the vortices using the shallow water equations, which describe a single layer of fluid that moves horizontally and has a free surface that moves up and down in response to fluid convergence and divergence. We find that the stability of the pattern depends mostly on shielding—an anticyclonic ring around each cyclone, but also on the depth. Too little shielding and small depth lead to merging and loss of the polygonal pattern. Too much shielding causes the cyclonic and anticyclonic parts of the vortices to fly apart. The stable polygons exist in between. Why Jupiter's vortices occupy this middle range is unknown. The budget—how the vortices appear and disappear—is also unknown, since no changes, except for an intruder that visited the south pole briefly, have occurred at either pole since *Juno* arrived at Jupiter in 2016.

Jupiter | vortex dynamics | *Juno* | shallow water model

With its unique pole-to-pole orbit, the *Juno* spacecraft was the first to view the geometric patterns of vortices at the poles of Jupiter. The spacecraft carries two imaging systems, JunoCam (1), a visible-light camera with broadband red, green, and blue filters, and JIRAM (2), the Jovian Infrared Auroral Mapper, whose imaging channel operates at 4.8- μ m wavelength. The spatial resolution over the pole is 50 km/pixel for JunoCam and 12 km/pixel for JIRAM (3, 4). JunoCam is sensitive to the colors and composition of the clouds, which are broadly distributed from 0.3 to 0.7 bars, and JIRAM is sensitive to holes in the clouds, which allow radiation from warmer levels at pressures up to 5 bars to reach the detector.

Fig. 1 shows views of the south pole by JunoCam and JIRAM. The figure shows five cyclonic vortices surrounding a central cyclonic vortex. At the north pole, there are eight cyclonic vortices surrounding a central cyclonic vortex. JunoCam is restricted to the sunlit side of the planet. The vortices last from one orbit to the next, 53 d later (5), so a visible-light mosaic of the entire polar region can be constructed from several orbital passes. JIRAM is sensitive to thermal emission from the planet and can view the entire pole during a single orbital pass.

Based on cloud markings, the cyclones' radii range from 2,000 to 3,500 km (4). Their centers are at latitudes of $\pm 83^\circ$, about 8,700 km from the respective poles. Based on azimuthal velocities, the cyclones' radii are $\sim 1,000$ km, i.e., the annulus of maximum wind is located $\sim 1,000$ km from the vortex centers, with peak speeds of 70 to 90 $\text{m}\cdot\text{s}^{-1}$ (4). Outside the peak, the wind profile

falls off faster than the $1/r$ dependence of a vortex patch surrounded by a region with zero vorticity—suggesting anticyclonic vorticity surrounding the cyclones. In other words, the cyclonic vortices are “shielded.” Shielding may explain the slow rotation (1.5° westward) of the structure as a whole during the 53 d of one orbit (5).

On Earth, cyclones drift poleward (6, 7), but they dissipate over land and cold ocean. Jupiter has neither land nor ocean, so the question is, why do cyclones neither accumulate at the poles nor merge? Saturn has only one cyclone, and it is surrounded by a sea of smaller anticyclones (8). Several theories (9–11) seem to account for the formation, poleward drift, and merging of cyclones on Saturn. Those models are constantly forced by small-scale short-lived processes that represent the effects of moist convection, but they do not produce polygonal patterns like those on Jupiter. In contrast, we initialize our calculations with fully formed polar cyclones arranged in polygonal patterns and we investigate their stability. We ask, what values of the input parameters lead to stable polygons on Jupiter as opposed to mergers transforming into one cyclone at each pole?

We model the vortices using the shallow water (SW) equations, which describe a single layer of fluid on a rotating sphere. It has nonlinear horizontal advection, planetary rotation, and an upper surface that moves up and down in response to convergence and divergence of the horizontal wind. Variations in the height of the upper surface produce the pressure gradients that accelerate the winds. The single layer rests hydrostatically on a much deeper isentropic layer at rest, and the system is the well-studied, reduced-gravity,

Significance

Like good wine, scientific problems gain significance as they age. Regular patterns of vortices have been studied theoretically and observed in the laboratory since the 19th century, but never before in a planetary atmosphere, with the complicating effects of planetary rotation, spherical geometry, and horizontal convergence and divergence. Instruments on the *Juno* spacecraft have given us the sizes and speeds of the vortices, but a true understanding requires a numerical model that matches the observations and simulates the long-term stability of the patterns. We provide such a model here, but the work is not done. We will make further progress as *Juno* continues its observations of this fascinating phenomenon.

Author contributions: C.L. and A.P.I. designed research; A.P.K. performed research and analyzed data; C.L., A.P.I., and H.B. contributed in discussion; and C.L. and A.P.I. wrote the paper.

The authors declare no competing interest.

This article is a PNAS Direct Submission.

Published under the PNAS license.

¹To whom correspondence may be addressed. Email: cli@gps.caltech.edu.

This article contains supporting information online at <https://www.pnas.org/lookup/suppl/doi:10.1073/pnas.2008440117/-DCSupplemental>.

First published September 8, 2020.

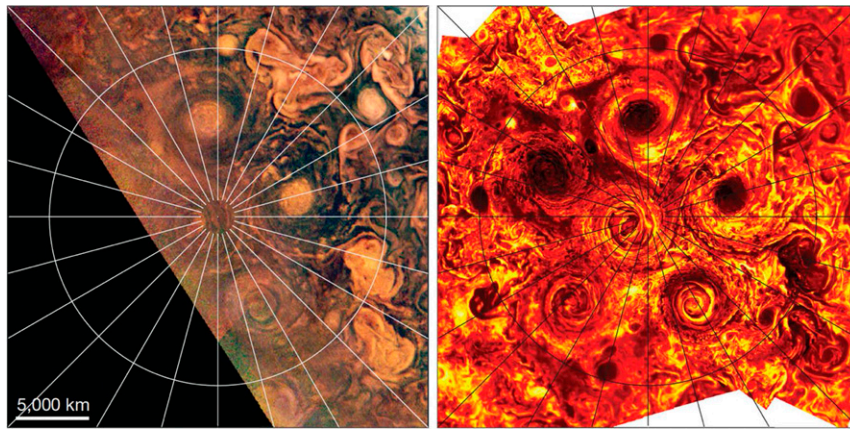


Fig. 1. South pole of Jupiter imaged by JunoCam (Left) and JIRAM (Right). The circle in each image is at latitude -80° . The five vortices at the vertices of the pentagon and the sixth vortex at the center are cyclones whose clockwise circulation is measured directly by tracking small clouds in sequences of images and inferred indirectly by the spiral tails trailing behind the general rotation. Clouds look bright in the JunoCam image, but they look dark in the JIRAM image because they are colder than the atmosphere below (3). Reprinted by permission from ref. 3, Springer Nature: [Nature](#), copyright (2018).

or $1\frac{1}{2}$ layer model (12, 13). Without rotation or convergence/divergence, the SW equations reduce to the two-dimensional (2D) Euler equations, which yield the barotropic vorticity equation and the $1/r$ falloff of velocity (Green's function) from a point vortex (14, 15). For large-scale, slowly varying flows in a rotating system, the Coriolis term is the dominant acceleration, as measured by the smallness of the Rossby number. Rotation and horizontal convergence/divergence add an intrinsic length scale, the radius of deformation L_d , which changes the falloff of velocity to the modified Bessel function K_1 (16, 17). The equations are known as the equivalent barotropic system. On a sphere, the decrease in the angle between the planet's rotation vector and the vertical unit vector as the latitude increases means that the total vorticity increases—becomes more cyclonic with latitude. The change of vorticity is called “beta,” and it causes cyclonic vortices to drift poleward and westward, often referred to as beta drift. Drifting vortices in the presence of a background vorticity gradient have been studied in rotating tank experiments (18), in atmospheres and oceans (19), and in ideal analytical settings (20, 21). Even on a sphere, beta drift does not occur if the ambient vorticity is irrotational (22). In other words, beta drift requires a vorticity gradient.

The interaction between vortices dates back to the 19th century and Kelvin's proof that a polygon of N identical point vortices arrayed symmetrically in a circle is stable only for $N < 7$ (23). However, adding a strong enough central vortex can stabilize a polygon consisting of arbitrarily many vortices (16, 24, 25). Single shielded vortices, i.e., vortices with $v = 0$ outside a certain radius, have various modes of instability (26), and they often break into tripoles (27), consisting of a central vortex of one sign and two satellite vortices of the opposite sign orbiting 180° apart. Tripoles are stable both in the barotropic and equivalent barotropic system (17, 28). Vortex crystals, in which many small vortices in random patterns spontaneously merge into geometric patterns of much larger vortices, are seen in laboratory experiments (14) and numerical simulations using the 2D Euler equations (29, 30). However, the 2D Euler equations do not have horizontal divergence, and they do not have a beta effect. Seeing how these additional parameters might apply in Jupiter's atmosphere is an important part of this paper.

For adiabatic inviscid flow on a rotating sphere, fluid elements conserve a quantity called potential vorticity (PV). For the shallow water equations, PV is $(\zeta + f)/h$, where $\zeta = (\nabla \times \mathbf{v}) \cdot \hat{\mathbf{k}}$ is the relative vorticity—the vertical component of the curl of the horizontal velocity, $f = 2\Omega \cos \theta$ is the planetary vorticity—the

vertical component due to the planet's rotation, Ω is the angular velocity of the planet, θ is colatitude, and h is the instantaneous depth of the fluid. The Rossby number Ro is $V/(fL)$, where V and L are a characteristic velocity and horizontal length scale, respectively. Taking the 80 m s^{-1} maximum velocity and the 1,000-km radius (4) of the vortices for V and L , one finds $Ro = 0.23$ when $f = 2\Omega$. The ratio ζ/f is exactly twice this value. The quasi-geostrophic (QG) approximation is based on $Ro \ll 1$ (31, 32), but the SW equations do not make this assumption. All of those aforementioned subsystems—QG, 2D Euler, point vortices—are limiting cases of the SW system.

The depth h is a measure of the stratification and is highly uncertain. Here, we use $\phi = gh$ as one of the two dependent variables, the other being the horizontal velocity \mathbf{v} . The gravity wave speed c is $\sqrt{\phi}$, and the radius of deformation L_d is c/f . For a thin layer of fluid floating hydrostatically on a much deeper layer, ϕ is gh multiplied by the fractional density difference between the two layers (12, 13). If c is independent of latitude, L_d will vary as $1/\cos(\theta)$. The corresponding estimates of L_d at the poles range from 350 km if the static stability is related to the difference between the dry and moist adiabatic lapse rates for a solar composition atmosphere and ~ 700 km if the water abundance is $4\times$ solar (33), to 700 to 1,000 km from vortex models and observations (34), to $\sim 1,300$ km from waves radiating from the Shoemaker-Levy impacts (35). This means the Burger number, $Bu = \phi_0/(fL)^2 = L_d^2/L^2$, could range from ~ 0.12 to ~ 1.7 based on the vortex radius of 1,000 km for L . In most cases, the lower part of this range ($Bu < 0.46$) cannot be reached because the depression of the upper surface at the center of the vortex is greater than the undisturbed depth, and the layer thickness goes to zero. Using a different value for L does not change our overall conclusion because the Rossby will also change proportionally, which cancels the effect.

In addition to the Rossby number and the Burger number, a third independent variable is θ , the initial colatitude of the vortices. It determines the value of $\beta = -\partial f/\partial \theta/R_J \approx 2\Omega \theta/R_J$ near the pole, where R_J is the radius of Jupiter. Note that $\beta = 0$ at the pole. The dimensionless number that gives the importance of β is $\beta L^2/V$. It compares β to the vorticity gradient associated with fluid motions, where L is the vortex radius as before. We take $\theta = L_p/R_J$, where L_p is the 8,700-km distance from the pole to the vortices, which are at 83° latitude. If $Ro = V/(fL) = 0.23$, we obtain $\beta L^2/V = LL_p/R_J^2/Ro = 0.0074$. It is a small number, about 10% of the midlatitude QG scaling, which lacks the L_p/R_J factor in the traditional β -plane approximation (31, 32), but it is

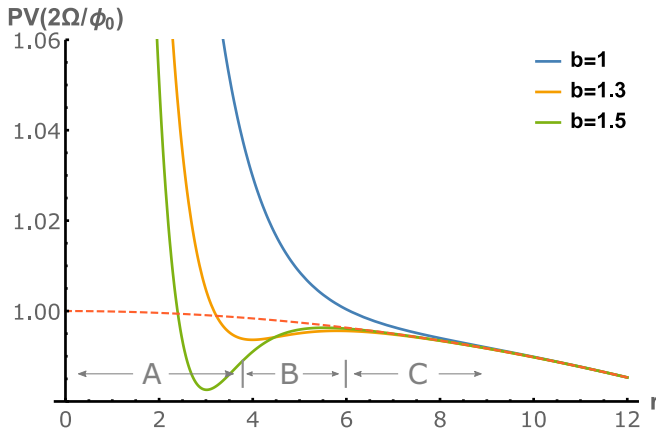


Fig. 2. Dimensionless potential vorticity (PV) profiles for different values of the steepness parameter b and three regions, A, B, and C, marked for the PV profile with $b = 1.3$ (for details, see the text). Larger values of b produce an annular band where the PV is less than the value at far-field and a local PV maximum outward. This annular band has anticyclonic vorticity, and it surrounds the central cyclone. The dimensionless planetary PV of an atmosphere at rest is plotted in the red dashed line with the pole at $r = 0$. The Rossby number $Ro = 0.2$ and the Burger number $Bu = 1$ are used for all of these profiles.

the precise reason why cyclonic vorticity is accumulated at the pole and why it may be offset by the vortex shielding resulted from the shape of the azimuthal wind profile.

The fourth independent variable comes from the initial velocity profile. Tropical cyclones on Earth either merge, drift apart, or orbit each other depending on their shielding (36–38). A simple expression for azimuthal velocity vs. radius, with a single parameter b that controls the amount of shielding, is as follows (37):

$$v(r) = v_m \left(\frac{r}{r_m} \right) \exp \left\{ \frac{1}{b} \left[1 - \left(\frac{r}{r_m} \right)^b \right] \right\}. \quad [1]$$

In some papers, b is known as the steepness parameter (28, 39) and is denoted by α . The azimuthal velocity profile has a single peak at $r = r_m$, reaching the velocity $v = v_m$. Fig. 2 shows dimensionless PV profiles for three different values of b and the background atmosphere at rest with the pole placed at $r = 0$, $PV = (\zeta + f)/\phi_0$, and

$$\zeta(r) = \frac{\partial v}{\partial r} + \frac{v}{r}, \quad \phi(r) = \phi_0 - \int_r^\infty \left[\frac{v^2}{r} + fv \right] dr. \quad [2]$$

In setting the initial conditions, we assume $f \approx 2\Omega$, in which case the integral can be done analytically using incomplete gamma functions. Velocity has been scaled by v_m , radial distance by r_m , and PV by $2\Omega/\phi_0$. The dimensionless planetary PV, shown by the dashed curve in Fig. 2, is $\cos(\theta)$. The vortices are northern hemisphere cyclones, which means they spin counter-clockwise as viewed from above. Relative vorticity is zero at infinity and is cyclonic (anticyclonic) where PV is greater than (less than) the value at infinity. The profiles with the larger values of b have shielding, i.e., anticyclonic relative vorticity surrounding the central cyclone. As calculated in *SI Appendix*, shielding always occur for profiles with $b > 1$, although it is negligible when b is small.

In the presence of beta, a shielded cyclone may create a local maximum of PV outside of its annular shielding, and two cyclones can either attract or repel depending on their relative positions.

Consider two cyclones, the first one is at rest, and the second one, an infinitely small test cyclone, moves under the influence of the first one. The test cyclone can be at three places: 1) inside of the radius of PV minimum, 2) outside of the radius of minimum PV but inside of the radius of local PV maximum, and 3) outside of the radius of local PV maximum, depicted respectively in Fig. 2. At positions 1 and 3, because the local PV gradient points to the center, the test cyclone will drift toward the center, displaying the attraction between vortices. Particularly, if the test cyclone is at position 1, mutual attraction will eventually lead to merging. However, at position 2, the local PV gradient points outward, and so the test cyclone will move away from the center as if it is repelled. Thus, the equilibrium position of the test cyclone is at the radius of PV maximum between 2 and 3 and the boundary between merging and separation is at the radius of PV minimum between 1 and 3. This is the result of a cyclone climbing up the vorticity gradient of the other (37, 38), which is the same process that makes tropical cyclones drift poleward and westward on Earth. Here, the mechanism of stability involves the interaction between the beta drift and the shielding, which is different from the interaction of two isolated vortices without beta (15).

Next, we will show, in our SW experiments, that shielded cyclones form stable polygons in a balance between the poleward drift due to the planetary beta effect and the repulsive drift due to the local PV gradient induced by other vortices. We find that the radius of PV minimum delineates the stability boundary very well as reasoned in the previous paragraph.

Results

Fig. 3 shows our determination of b obtained by fitting the function $v(r)$ in Eq. 1 to the observed velocity profiles in figure 6 A and B of ref. 4. We use the WebPlotDigitizer (<https://automeris.io/WebPlotDigitizer/>) to digitize the figures. The result is $b \approx 1.5 \pm 0.2$. Values of 1.0 and 2.0 for b are decidedly out of range, and the 0.2 uncertainty is an eyeball estimate. Nevertheless, we shall see that the observed velocity profile confirms that the Jovian vortices may be shielded to some extent.

Fig. 4 is a series of six frames from *Movie S1* that shows a configuration like that at the south pole of Jupiter—five cyclones circling a cyclone at the pole, and an intruder. The simulation is

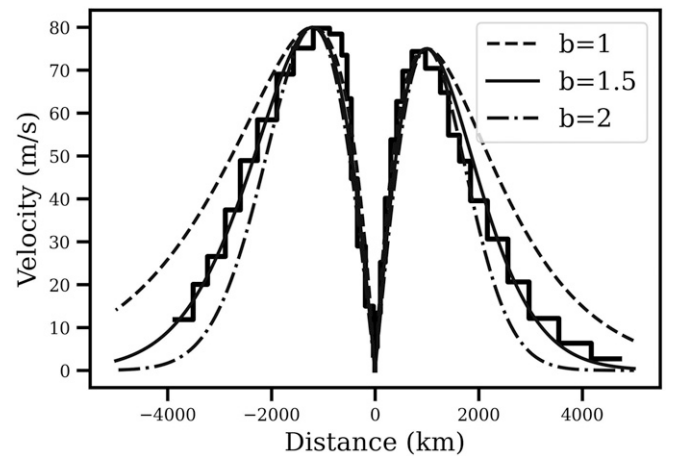


Fig. 3. Fitting to the observed velocity profiles of Jovian polar vortices. Black step: averaged velocity profiles of north polar cyclones (right half) and south polar cyclones (left half). Dashed, solid, and dash-dotted lines: velocity profiles given by $b = 1$, $b = 1.5$, and $b = 2$ in Eq. 1, respectively. The radius of the north polar cyclones (r_m) are 1,000 km, and the radius of the south polar cyclones are 1,200 km.

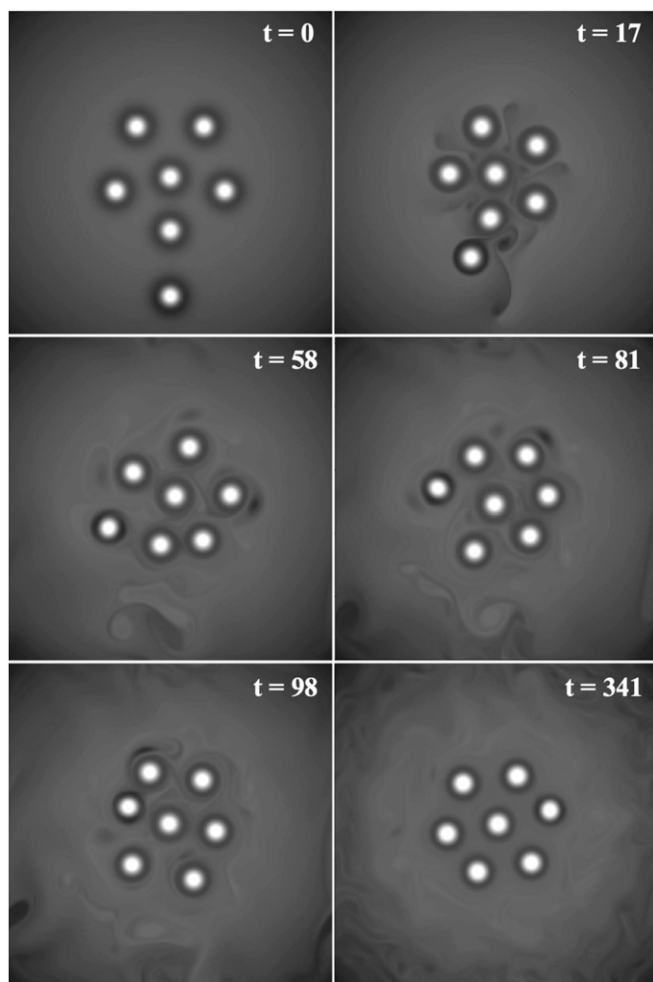


Fig. 4. Frames from [Movie S1](#) with Burger number $Bu = 10$, steepness parameter $b = 1.5$, Rossby number $Ro = 0.23$, and initial polygon vertices at 83° latitude. The intruder is initially at 70° , but it drifts poleward and westward under the influence of beta effect. Time is given in each frame in units of days.

for the northern hemisphere, so the cyclones spin counterclockwise. The cyclones are identical to each other and have dimensions and speeds taken from observation (4, 5). The value of b is 1.5, in agreement with our estimate based on the observations in Fig. 3, Ro is 0.23, and Bu is 10. The shading in the figure is PV, with cyclonic regions bright and anticyclonic regions dark. The vortices are initially at 83° latitude. Since PV is a conserved tracer, it accurately shows the motion of fluid elements. [Movie S1](#) shows the relatively rapid azimuthal motion around each cyclone and the much slower motion of the intruder toward the pole. This difference in speeds is consistent with β going to zero at the pole. The movie and the six frames of Fig. 4 show the intruder circling clockwise around the ring as if it were trying to get in, until it succeeds and turns the pentagon into a hexagon. The hexagon lasts for the length of the integration, 500 simulated days. Having an intruder in Fig. 4 is based on observation: Around Perijove 13, a cyclone from outside the south polar pentagon pushed into the structure, temporarily making it a hexagon, but the intruder was soon pushed out (40).

Fig. 5 is the same as Fig. 4 except there is no intruder and the initial velocity profile of each cyclone has $b = 1$ and $Bu = 2$. These vortices are only marginally shielded according to Fig. 2. [Movie S2](#) shows the central cyclone spiraling outward in

a clockwise direction, increasing its distance from the pole until it reaches the cyclones that form the pentagon and merges with one of them. This spiraling is an instability of the structure and is not just a merger of a cyclone pair. The new combined cyclone merges with another cyclone, and the mergers continue. Other movies in [SI Appendix](#) show a series with $Bu = 1$ and several values of b . For $b = 1.5$ ([Movie S3](#)), the pentagon contracts by about 3.7% and equilibrates at 83.3° latitude, agreeing even better to the observed positions of the cyclones (3). The central vortex begins spiraling, but the structure is stable. For $b = 2.25$ ([Movie S4](#)), 3.00 ([Movie S5](#)), and 3.75 ([Movie S6](#)), the pentagonal structure remains but the shielded cyclones turn into tripoles. The contraction of the structure slightly increases with the increase of b by up to 7%. Cases with $Bu = 10$ and the same values of b are essentially the same, although for $b = 3$ ([Movie S7](#)) the vortices collide during the contraction phase and the satellites lose a large fraction of their original material. Some of that is reabsorbed and some of it drifts away. However, the cases $b = 4$ and $Bu = 2$ ([Movie S8](#)) and 5 ([Movie S9](#)) are different—the tripoles disintegrate and the remnants of the shields, because they are anticyclonic, drift off to lower latitudes and the polygonal structure is destroyed.

Fig. 6 shows a summary of SW results in the b - Bu plane. Each point is a movie listed in [SI Appendix](#), summarized in [SI Appendix, Table S1](#), and the symbols are as follows: 1) unshielded

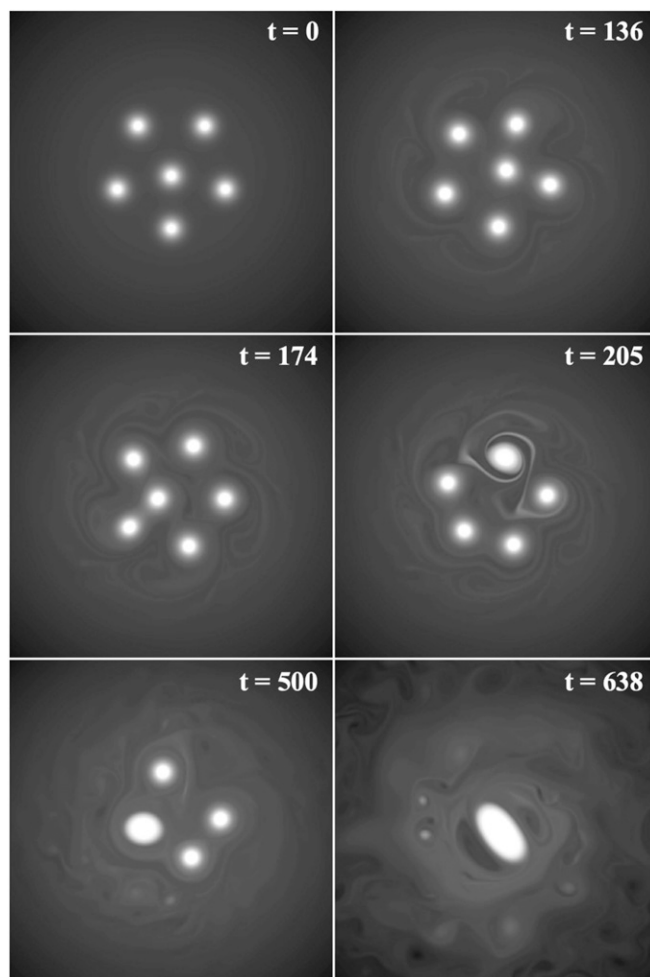


Fig. 5. Similar to Fig. 4, except $Bu = 2$, $b = 1$ ([Movie S2](#)), and there is no intruder.

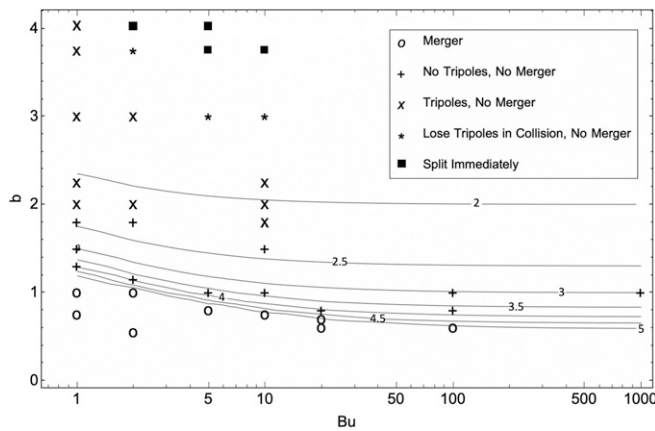


Fig. 6. Regime diagram classifying the behavior of the cyclone patterns for 30 runs of the SW model. Each point is a 500-d simulation and reflects the type of behavior for a particular value of Burger number Bu and steepness parameter b . The contours give the initial distance from the center of each cyclone to the annulus of minimum PV. The contour labels have units of r_m , which is the radius of maximum initial azimuthal velocity. The Rossby number is between 0.2 and ~ 0.23 to match observations.

vortices that merge, 2) shielded vortices that retain their polygonal pattern and their axisymmetric shields, 3) shielded vortices that turn into tripoles but retain their polygonal pattern, 4) shielded vortices whose tripoles partly disintegrate although the polygonal pattern remains, and 5) tripoles that disintegrate such that the polygonal pattern is lost. The contour lines in Fig. 6 give the radii where PV has its minimum value (Fig. 2). A minimum-PV radius of 4.5 clearly divides the boundary between regions 1 and 2. That line is a better fit than a single value of b , and reflects the influence of Bu on the results. The stability boundary $r = 4.5$ is slightly larger than the minimum-PV radius shown in Fig. 2 for $b = 1.3$ probably due to the finite size of the vortices. The vortices in Fig. 5, with $b = 1$ and $Bu = 2$, lie just below the line, consistent with the observed merging. A minimum-PV radius of 2.2 divides regions 2 and 3. The boundary between regions 3 and 4 does not coincide with a minimum-PV radius. For $b = 3$ and $b = 4$, it seems to lie between $Bu = 1$ and $Bu = 10$, with the former more stable

than the latter. This could have more to do with pattern contraction and vortex collisions than with tripole stability.

The limit $Bu \rightarrow \infty$ corresponds to infinite radius of deformation, where the flow becomes 2D and incompressible. A 2D incompressible numerical model (28, 39), which is the same as the 2D Euler equations, says that the transition from axisymmetric shielded cyclones to tripoles occurs at $b = 1.85$, which agrees with the points at large Bu in Fig. 6. That numerical model (28) says that the tripoles disintegrate above $b = 4$, which also agrees with Fig. 6. The observed value $b = 1.5 \pm 0.2$ agrees with the SW results in Fig. 6 in that it is located in region 2 where polygons are stable and the vortices do not have tripoles.

Discussion

We have investigated the stability of polygonal patterns of polar cyclones on Jupiter, and we have shown that the polygons most likely owe their stable structure to shielding. Vortices in polygonal patterns is an old subject, but the complications of beta drift and polar geometry are new. There are many questions we have not answered. We have not explored how the cyclones form—whether they form in place or drift up from lower latitudes. Additionally, we have not explained how a steady state is maintained—why the number of cyclones does not increase with time. Furthermore, we have not determined how shielding develops, or why only the Jovian vortices are shielded. We have not varied the Rossby number because it is constrained by observation. Moreover, at the poles, the limit $Ro \rightarrow 0$ has a singular effect on the importance of beta. Finally, we have not explored 3D effects and thermal structure except to postulate that there is a finite radius of deformation. Its value is currently uncertain, but further measurement of the physical properties and time evolution may help place the Jovian vortices more precisely in the SW parameter space.

Data Availability. All movies, codes, and data used to generate figures and tables in the paper have been deposited in GitHub (<https://github.com/chengcli/2020.JupiterPolarVortex>). All study data are included in the article and *SI Appendix*.

ACKNOWLEDGMENTS. This research was carried out at the California Institute of Technology under a contract with the National Aeronautics and Space Administration (NASA), Grant/Cooperative Agreement 80NSSC20K0555, and a contract with the *Juno* mission, which is administered for NASA by the Southwest Research Institute. C.L. was supported by the 51 Peg b Postdoctoral Fellowship sponsored by the Heising-Simons Foundation.

1. C. J. Hansen et al., Junocam: Juno's outreach camera. *Space Sci. Rev.* **213**, 475–506 (2017).
2. A. Adriani et al., JIRAM, the Jovian infrared auroral mapper. *Space Sci. Rev.* **213**, 393–446 (2017).
3. A. Adriani et al., Clusters of cyclones encircling Jupiter's poles. *Nature* **555**, 216–219 (2018).
4. D. Grassi et al., First estimate of wind fields in the Jupiter polar regions from JIRAM–Juno images. *J. Geophys. Res. Planets* **123**, 1511–1524 (2018).
5. F. Tabataba-Vakili et al., Long-term tracking of circumpolar cyclones on Jupiter from polar observations with JunoCam. *Icarus* **335**, 113405 (2020).
6. J. Chan, R. Williams, Analytical and numerical studies of the beta-effect in tropical cyclone motion. 1. Zero mean flow. *J. Atmos. Sci.* **44**, 1257–1265 (1987).
7. L. Oruba, G. Lapeyre, G. Riviere, On the poleward motion of midlatitude cyclones in a baroclinic meandering jet. *J. Atmos. Sci.* **70**, 2629–2649 (2013).
8. U. A. Dyudina et al., Saturn's south polar vortex compared to other large vortices in the solar system. *Icarus* **202**, 240–248 (2009).
9. M. E. O'Neill, K. A. Emanuel, G. R. Flierl, Polar vortex formation in giant-planet atmospheres due to moist convection. *Nat. Geosci.* **8**, 523–U118 (2015).
10. M. E. O'Neill, K. A. Emanuel, G. R. Flierl, Weak jets and strong cyclones: Shallow-water modeling of giant planet polar caps. *J. Atmos. Sci.* **73**, 1841–1855 (2016).
11. S. R. Brueshaber, K. M. Sayanagi, T. E. Dowling, Dynamical regimes of giant planet polar vortices. *Icarus* **323**, 46–61 (2019).
12. R. Mied, G. Lindemann, Propagation and evolution of cyclonic gulf-stream rings. *J. Phys. Oceanogr.* **9**, 1183–1206 (1979).
13. E. Chassignet, B. Cushmanroisin, On the influence of a lower layer on the propagation of nonlinear oceanic eddies. *J. Phys. Oceanogr.* **21**, 939–957 (1991).
14. K. S. Fine, A. C. Cass, W. G. Flynn, C. F. Driscoll, Relaxation of 2D turbulence to vortex crystals. *Phys. Rev. Lett.* **75**, 3277–3280 (1995).
15. X. Carton, On the merger of shielded vortices. *Europhys. Lett.* **18**, 697–703 (1992).
16. G. Morikawa, E. Swenson, Interacting motion of rectilinear geostrophic vortices. *Phys. Fluids* **14**, 1058 (1971).
17. Z. Kizner, Stability of point-vortex multipoles revisited. *Phys. Fluids* **23**, 064104 (2011).
18. G. F. Carnevale, R. C. Kloosterziel, G. J. F. Van Heijst, Propagation of barotropic vortices over topography in a rotating tank. *J. Fluid Mech.* **233**, 119–139 (1991).
19. D. B. Chelton, M. G. Schlax, R. M. Samelson, Global observations of nonlinear meso-scale eddies. *Prog. Oceanogr.* **91**, 167–216 (2011).
20. S. G. L. Smith, The motion of a non-isolated vortex on the beta-plane. *J. Fluid Mech.* **346**, 149–179 (1997).
21. G. R. Flierl, Isolated eddy models in geophysics. *Annu. Rev. Fluid Mech.* **19**, 493–530 (1987).
22. M. I. Jamalooddeen, P. K. Newton, The N-vortex problem on a rotating sphere. II. Heterogeneous platonic solid equilibria. *Proc. R. Soc. A Math. Phys. Eng. Sci.* **462**, 3277–3299 (2006).
23. W. Thomson, Floating magnets. *Nature* **18**, 13–14 (1878).
24. G. Mertz, Stability of body-centered polygonal configurations of ideal vortices. *Phys. Fluids* **21**, 1092–1095 (1978).
25. H. Aref, Integrable, chaotic, and turbulent vortex motion in two-dimensional flows. *Annu. Rev. Fluid Mech.* **15**, 345–389 (1983).
26. G. Flierl, On the instability of geostrophic vortices. *J. Fluid Mech.* **197**, 349–388 (1988).

27. G. Vanheijst, R. Kloosterziel, C. Williams, Laboratory experiments on the tripolar vortex in a rotating fluid. *J. Fluid Mech.* **225**, 301–331 (1991).
28. X. Carton, G. Flierl, L. Polvani, The generation of tripoles from unstable axisymmetric isolated vortex structures. *Europhys. Lett.* **9**, 339–344 (1989).
29. D. A. Schecter, D. H. E. Dubin, K. S. Fine, C. F. Driscoll, Vortex crystals from 2D Euler flow: Experiment and simulation. *Phys. Fluids* **11**, 905–914 (1999).
30. J. Jimenez, A. Guegan, Spontaneous generation of vortex crystals from forced two-dimensional homogeneous turbulence. *Phys. Fluids* **19**, 085103 (2007).
31. J. R. Holton, G. Hakim, *An Introduction to Dynamic Meteorology*, (Academic Press, ed. 5, 2013).
32. G. K. Vallis, *Atmospheric and Oceanic Fluid Dynamics*, (Cambridge University Press, 2006).
33. R. Achterberg, A. Ingersoll, A normal-mode approach to Jovian atmospheric dynamics. *J. Atmos. Sci.* **46**, 2448–2462 (1989).
34. M. H. Wong, I. de Pater, X. Asay-Davis, P. S. Marcus, C. Y. Go, Vertical structure of Jupiter's Oval BA before and after it reddened: What changed? *Icarus* **215**, 211–225 (2011).
35. H. B. Hammel *et al.*, HST imaging of atmospheric phenomena created by the impact of comet Shoemaker-Levy 9. *Science* **267**, 1288–1296 (1995).
36. S. Chang, A numerical study of the interactions between 2 tropical cyclones. *Mon. Weather Rev.* **111**, 1806–1817 (1983).
37. M. Demaria, J. Chan, A numerical study of the interactions between 2 tropical cyclones. *Mon. Weather Rev.* **112**, 1643–1645 (1984).
38. S.-E. Shin, J.-Y. Han, J.-J. Baik, On the critical separation distance of binary vortices in a nondivergent barotropic atmosphere. *J. Meteorol. Soc. Jpn.* **84**, 853–869 (2006).
39. X. Carton, B. Legras, The life-cycle of tripoles in 2-dimensional incompressible flows. *J. Fluid Mech.* **267**, 53–82 (1994).
40. A. Adriani *et al.*, Two-year observations of the Jupiter polar regions by JIRAM on board *Juno*. *J. Geophys. Res.* **125**, e2019JE006098 (2020).